

High-resolution dynamic susceptibility contrast perfusion imaging using higher-order temporal smoothness regularization

Julia V. Velikina¹  | Youngkyoo Jung² | Aaron S. Field¹ | Alexey A. Samsonov¹ 

¹Department of Radiology, University of Wisconsin-Madison, Madison, Wisconsin USA

²Department of Radiology, University of California-Davis, Davis, California USA

Correspondence

Julia V. Velikina, Department of Radiology, University of Wisconsin-Madison, WIMR, 1111 Highland Ave., Rm. 1117, Madison, WI 53705, USA.

Email: velikina@wisc.edu

Funding information

National Institutes of Health, Grant/Award Numbers: P30CA014520, R01EB027087, R21EB018483

Purpose: To improve image quality and resolution of dynamic susceptibility contrast perfusion weighted imaging (DSC-PWI) by developing acquisition and reconstruction methods exploiting the temporal regularity property of DSC-PWI signal.

Theory and Methods: A novel regularized reconstruction is proposed that recovers DSC-PWI series from interleaved segmented spiral k -space acquisition using higher order temporal smoothness (HOTS) properties of the DSC-PWI signal. The HOTS regularization is designed to tackle representational insufficiency of the standard first-order temporal regularizations for supporting higher accelerations. The higher accelerations allow for k -space coverage with shorter spiral interleaves resulting in improved acquisition point spread function, and acquisition of images at multiple TEs for more accurate DSC-PWI analysis.

Results: The methods were evaluated in simulated and in-vivo studies. HOTS regularization provided increasingly more accurate models for DSC-PWI than the standard first-order methods with either quadratic or robust norms at the expense of increased noise. HOTS DSC-PWI optimized for noise and accuracy demonstrated significant advantages over both spiral DSC-PWI without temporal regularization and traditional echo-planar DSC-PWI, improving resolution and mitigating image artifacts associated with long readout, including blurring and geometric distortions. In context of multi-echo DSC-PWI, the novel methods allowed $\sim 4.3\times$ decrease of voxel volume, providing $2\times$ number of TEs compared to the previously published results.

Conclusions: Proposed HOTS reconstruction combined with dynamic spiral sampling represents a valid mechanism for improving image quality and resolution of DSC-PWI significantly beyond those available with established fast imaging techniques.

KEYWORDS

compressed sensing, dynamic susceptibility contrast perfusion weighted imaging, spiral imaging, temporal regularization

1 | INTRODUCTION

MRI-based dynamic susceptibility contrast (DSC) perfusion weighted imaging (PWI)¹ can estimate essential brain perfusion parameters, which have significant utility in many clinical applications. DSC-PWI may inform the diagnosis of transient ischemic attack² and assess “tissue-at-risk” in acute stroke patients.³ In brain tumor patients, DSC-PWI parameters have been used to differentiate between glioma grades,⁴ to distinguish between recurring tumors and treatment effects,⁵ and to evaluate the response to anti-angiogenesis drug therapy.^{6,7} Among the various hemodynamic parameters that may be estimated with DSC-PWI, relative cerebral blood volume (rCBV) in particular has been prognostic in patients with high-grade glioma.⁸

DSC-PWI faces several challenges in acquisition and interpretation of the data, which existing methods can mitigate only partially. The acquisition must capture rapid dynamic $T2^*$ changes caused by the passage of the intravenously administered contrast agent (CA) bolus, calling for imaging at high (near-second) temporal resolution, typically attained at the expense of spatial resolution and coverage. Next, the longer TE is required to sensitize signal to $T2^*$ values present in tissue, but much shorter TE is simultaneously desirable to avoid errors in the arterial input function (AIF) and, hence, in the quantitative perfusion analysis.⁹ Additional errors may arise in tumor imaging, where leaky vasculature leads to CA accumulation in the extravascular space, shortening $T1$ relaxation time and introducing signal dependencies unaccounted for by DSC-PWI models.^{10,11} Multi-echo DSC-PWI imaging demonstrated significant promise to mitigate these errors^{12–14} by virtue of direct dynamic $T2^*$ mapping, thereby eliminating the $T1$ effects from the analysis,^{15,16} and permitting optimization of individual TEs for AIF and tissue. However, collecting images at several TEs to address the above issues makes DSC-PWI even more data-demanding, further exacerbating its resolution and coverage limitations.

The standard DSC-PWI acquisition approach is single-shot EPI, which reaches the required imaging speed at the expense of image quality degradations. Higher resolution EPI is hampered by point spread function (PSF) widening due to the $T2^*$ decay during its long readout. The long readout also leads to prominent geometric image distortions and signal voids. These effects may be somewhat alleviated using non-Cartesian trajectories that cover k -space more efficiently, e.g., single-shot spirals.¹⁷ However, limitations of the single-shot acquisition pertain to spiral imaging as well,¹⁸ further emphasizing that a more efficient sampling alone cannot improve existing

tradeoffs between imaging speed and image quality in DSC-PWI.

Acquisition and reconstruction are tightly coupled in the context of fast imaging and require a simultaneous design for optimal results. In the case of DSC-PWI, segmenting k -space acquisition over N repetitions can be used to shorten readout and gain improvements in image quality and resolution, but only at the expense of the corresponding N -fold reduction in temporal resolution. To preserve temporal resolution, the reconstruction should be able to restore an image from each individual shot (i.e., from N -fold undersampled data); therefore, an upper bound on the associated image quality improvement is set by the undersampling level manageable by a given reconstruction technique. For example, a combination of multi-shot EPI and parallel imaging can reduce $T2^*$ blurring and susceptibility distortions¹² but only moderately, given the relatively low accelerations attainable with parallel imaging.¹⁹ In some dynamic MRI applications, additional accelerations were attained using various assumptions about temporal signal behavior.²⁰ For example, exploiting temporal signal modeling has empowered accelerated cardiac perfusion and functional imaging,²¹ with particularly promising results achieved by a combination of compressed sensing (CS) methods with non-Cartesian sampling trajectories, e.g., spiral and radial.^{22–24} Yet, the utility of similar approaches for DSC-PWI remains unclear, especially in a view of representational insufficiency of the standard models (e.g., in total variation [TV]-based temporal regularization),²⁵ which may limit achievable accelerations in applications with rapidly varying temporal dynamics such as DSC-PWI.

In this work, we present a novel approach to high-resolution, high-quality DSC-PWI based on the multi-shot, multi-echo spiral acquisition. The multi-shot sampling with shorter readout is made possible by a combination of spiral interleaves, pseudo-randomly distributed in time, and a reconstruction tailored to support the high undersampling levels of such acquisition. For the latter, we propose a regularized method that exploits higher order smoothness properties of the DSC-PWI temporal signal to attain the required performance, as compared to the standard first-order temporal regularization methods.^{22,23,26} To solve the problem of $B0$ blurring afflicting the spiral imaging, we enhance our reconstruction with time segmented $B0$ correction, for which the $B0$ map is estimated from the multi-echo data themselves. In the following, we describe the rationale for the proposed acquisition and reconstruction approaches, validate them in simulations and in vivo data, and compare the proposed method with clinical DSC-PWI.

2 | THEORY

2.1 | Problem formulation

MRI signal detected by a receiver coil with sensitivity profile $C(\mathbf{r})$ at time t is given by

$$\tilde{s}(t) = \int_{\text{ROI}} C(\mathbf{r}) \tilde{f}(\mathbf{r}) e^{(R_2^*(\mathbf{r}) + i\omega(\mathbf{r}))(t + TE)} e^{-2\pi i \langle \mathbf{k}(t), \mathbf{r} \rangle} d\mathbf{r}, \quad (1)$$

where $\tilde{f}(\mathbf{r})$ is a continuous function of the object's transverse magnetization at location \mathbf{r} immediately after radiofrequency excitation, $R_2^* = 1/T_2^*$ is the observed transverse relaxation rate, $\omega(\mathbf{r})$ is the main field inhomogeneity, time variable t is defined with respect to the echo time TE , and $\mathbf{k}(t)$ is the k-space trajectory.²⁷ Absorbing contributions of $R_2^*(\mathbf{r})$ and $\omega(\mathbf{r})$ at TE into a signal function,

$$f(\mathbf{r}) = \tilde{f}(\mathbf{r}) e^{(R_2^*(\mathbf{r}) + i\omega(\mathbf{r}))TE}, \quad (2)$$

and ignoring $R_2^*(\mathbf{r})$ decay during the readout, we can simplify the signal equation as follows:

$$\tilde{s}(t) = \int_{\text{ROI}} C(\mathbf{r}) f(\mathbf{r}) e^{i\omega(\mathbf{r})t} e^{-2\pi i \langle \mathbf{k}(t), \mathbf{r} \rangle} d\mathbf{r}. \quad (3)$$

(The effects of this standard simplification in the context of the proposed multi-echo acquisition are explored further in the paper.) The field map contributions remain explicitly accounted for, which permits deblurring with pre-measured B_0 field map in non-Cartesian acquisitions.²⁷

MRI signal is sampled at the discrete time points t_m , with acquired data contaminated by identically independently distributed (i.i.d.) complex Gaussian noise η_m :

$$s_m = \tilde{s}(t_m) + \eta_m$$

Following the formalism of Ref.²⁷, we can represent the sought magnetization vector in the basis of Dirac delta functions:

$$f(\mathbf{r}) = n \sum f_n \delta(\mathbf{r} - \mathbf{r}_n),$$

which, when substituted into the signal equation, leads to

$$\tilde{s}(t) = n \sum C(\mathbf{r}_n) f_n e^{i\omega_n t} e^{-2\pi i \langle \mathbf{k}(t), \mathbf{r}_n \rangle}, \quad (4)$$

and then to the matrix formulation of the forward problem:

$$\mathbf{s} = \mathbf{E}\mathbf{f} + \boldsymbol{\eta} \quad (5)$$

Here, the column vector \mathbf{s} contains the sampled data, and the entries of the encoding matrix \mathbf{E} are given by

$$E_{m,n} = C(\mathbf{r}_n) e^{i\omega_n t_m} e^{-2\pi i \langle \mathbf{k}(t_m), \mathbf{r}_n \rangle}.$$

In the case of single-coil acquisition, the coil sensitivity term $C(\mathbf{r})$ can be absorbed into the magnetization vector in Equation (2). In the case of multi-coil acquisition, \mathbf{s} represents a column vector comprising stacked data vectors from all coil channels, and the encoding matrix is expanded using the known coil sensitivities following the conventions of Ref.²⁸ In dynamic imaging, MR signal can be expressed in a similar form as

$$\bar{\mathbf{s}} = \bar{\mathbf{E}}\bar{\mathbf{f}} + \bar{\boldsymbol{\eta}}, \quad (6)$$

where the vectors contain stacked single image counterparts from all time frames, and the block-diagonal encoding matrix $\bar{\mathbf{E}}$ contains the encoding matrices from individual time frames on its main diagonal, all reflected by the overbar in the notation. Noise-optimized reconstruction of the time series can be achieved by enforcing consistency with the data in the least squares sense:

$$\bar{\mathbf{f}} = \arg \min_{\bar{\mathbf{f}}} \|\bar{\mathbf{E}}\bar{\mathbf{f}} - \bar{\mathbf{s}}\|_2, \quad (7)$$

where $\|\cdot\|_2$ is the ℓ_2 norm, an instance of ℓ_p norm defined in general form as

$$\|x\|_p = \left(\sum |x_i|^p \right)^{1/p}, p \geq 1. \quad (8)$$

While the estimation is typically well-posed for fully sampled or moderately undersampled (in case of multi-coil formulation) data, reducing the sampling density to gain spatial and/or temporal resolution deteriorates conditioning of the inversion problem leading to aliasing and noise amplification. To alleviate these, the data fidelity term can be augmented by penalty terms \mathfrak{R}_j that regularize inversion:

$$\bar{\mathbf{f}} = \arg \min_{\bar{\mathbf{f}}} \left(\|\bar{\mathbf{E}}\bar{\mathbf{f}} - \bar{\mathbf{s}}\|_2^2 + j \sum \lambda_j \mathfrak{R}_j(\bar{\mathbf{f}}) \right), \quad (9)$$

with the regularization coefficients λ_j providing balance among them. The regularizers are given by

$$\mathfrak{R}_j x = |\Psi_j x|_{X_j} \quad (10)$$

Here, Ψ_j are operators whose design is guided by prior information (i.e., signal model), and whose effect is measured by norms or semi-norms in spaces X_j . The norm is usually chosen to be ℓ_2 for noise-optimal reconstruction (as it provides maximum a posteriori estimation [MAP]

under the assumption of Gaussian noise²⁹), or ℓ_1 for promoting sparsity³⁰ in CS MRI.³¹ Provided that $\Psi_j x$ is a sparse vector, the latter is more forgiving to deviations of signal from the model than the former, thereby introducing less bias towards the model.

As a rule, increasing the degree of data undersampling biases the solution towards the regularizing model; therefore, a proper selection of the regularizers is critical for highly accelerated imaging. The lack of an appropriate model, for example, confines spatially regularized techniques to low accelerations before reconstruction accuracy is affected.³² Temporal regularization (i.e., when Ψ_j act in the temporal dimension only) has demonstrated promise to enable higher accelerations. The temporal variation models often may be learned from the data themselves (e.g., in the form of a low-rank representation) if a subset of k-space locations is sampled repeatedly,^{33,34} but such trajectory designs affect acquisition efficiency. In the following, we assume that such a model is not available and use general knowledge about the signal behavior in the temporal dimension.

2.2 | Higher-order temporal smoothness (HOTS) regularization

The signal in DSC-PWI can be assumed to vary smoothly in the temporal dimension. Indeed, the gradient echo-based acquisition causes the signal to follow the change in T_2^* -relaxation rate, ΔR_2^* , with respect to its value prior to the CA injection exponentially:

$$f(\mathbf{r}, t) = f(\mathbf{r}, 0)e^{-TE \cdot \Delta R_2^*(\mathbf{r}, t)}, \quad (11)$$

which, in turn, relates nearly linearly to tissue CA concentration $C_t(t)$ ³⁵:

$$\Delta R_2^* \propto C_t(t) \quad (12)$$

The latter can be modeled as

$$C_t(t) = CBF \cdot (C_A(t) \times r(t)), \quad (13)$$

where $C_A(t)$ is AIF, CBF is the cerebral blood flow, $r(t)$ a tissue residue function representing the fraction of CA in the tissue vasculature at time t ,³⁶ and $*$ denotes convolution operation. Since $C_A(t)$ can be represented as a linear combination of infinitely differentiable gamma variate functions,³⁷ its convolution with a bounded function $r(t)$ ensures that $C_t(t)$ and, hence, the signal curve (Equation 11) is at least as smooth (i.e., has the same number of derivatives).

For purposes of the regularization design, it is convenient to think that the signal curve belongs to a space

of functions possessing sufficiently many derivatives and equipped with a norm that measures both the size and regularity of a function. In mathematical terms, it belongs to the Sobolev space of functions W_p^d ,³⁸ i.e., whose $(d-1)^{st}$ derivative is absolutely continuous and whose d^{th} derivative raised to the power $p \geq 1$ has a finite integral. (The latter implies that the function belongs to the space L_p , a continuous counterpart of ℓ_p (Equation 8), equipped with the norm $\|x\|_p = (\int |x(t)|^p dt)^{1/p}$). It is an established result that functions belonging to the Sobolev space are best described by piecewise polynomials (splines) of order d in the sense that they minimize the worst-case error of such signal approximation from finite measurements.³⁸⁻⁴¹ In other words, in the absence of more specific modeling information about the signal behavior in the temporal dimension other than its differentiability, such functions can best be locally represented by polynomials of order d . In turn, it suggests that the discrete differential operator Δ^d annihilating the polynomials of order d is the natural choice as a penalty functional for a class of d -times differentiable functions.

We should point out that the reasoning above rationalizes the common use of the first difference ($d = 1$) (e.g., in temporally constrained ($p = 2$)²⁶ or TV-based CS ($p = 1$) reconstructions^{22,23}), but does not necessarily limit the order of the differential operator in the regularizers. It is reasonable to assume that for applications with rapid contrast dynamics, modeling it with higher order polynomials ($d > 1$) may provide a more accurate model for reconstruction of the undersampled DSC-PWI data. We will explore it further in the paper, along with effects of the higher order differential operators on the noise performance of the reconstruction. An additional aspect, considered in our regularization design, that affects both accuracy and noise performance is the selection of the regularizing norms in Equation (10), with ℓ_1 norm favoring the former and ℓ_2 norm optimizing the latter.

3 | METHODS

3.1 | Image reconstruction algorithm

We solve the problem in Equation (9) using iteratively reweighted least squares method that converges to a solution of a general ℓ_p problem through a series of ℓ_2 sub-problems⁴² with n^{th} iteration solving:

$$\bar{\mathbf{f}}^{(n+1)} = \arg \min_{\mathbf{f}} \left(\|\bar{\mathbf{E}}\mathbf{f} - \bar{\mathbf{s}}\|_2^2 + \|\mathbf{W}_n \Delta^d \bar{\mathbf{f}}\|_2^2 \right) \quad (14)$$

where \mathbf{W}_n is a diagonal reweighting matrix updated according to the chosen norm in the regularization term

(Equation 10) and Δ^d is a discrete difference operator acting pixelwise in the temporal dimension. For a temporal waveform x , operator is defined recursively using forward differences as follows:

$$\Delta x_i = x_{i+1} - x_i, \quad \Delta^d x = \Delta (\Delta^{d-1} x), \quad d > 1.$$

For ℓ_2 norm, the reweighting matrix is the identity. For ℓ_1 norm, the exact updates are given by

$$\text{diag}(\mathbf{W}_n) = \left| \Delta^d \bar{\mathbf{f}}^{(n)} \right|^{-1/2}. \quad (15)$$

The singularity of the updates for small residual values can be mitigated either by truncation or by selecting a modified variant of ℓ_1 norm. In this paper, we select a norm defined in Ref.⁴³ as

$$\|x\|_{\ell_1/\ell_2} = \sum_i \left(\sqrt{1 + |x_i/\sigma|^2} - 1 \right). \quad (16)$$

This function is a smooth approximation of the Huber loss function, which is strongly convex when close to the minimum, while providing ℓ_1 behavior for larger values, ensuring continuous derivatives and making the minimization problem well-posed.⁴⁴ The sequence of corresponding reweighting matrices is given by

$$\text{diag}(\mathbf{W}_n) = \left(\left| \Delta^d \bar{\mathbf{f}}^{(n)} \right|^2 + \sigma_n^2 \right)^{-1/2}, \quad \mathbf{W}_1 = Id. \quad (17)$$

One reasonable choice for the parameter σ is

$$\sigma_n = 0.6 \cdot \text{std} \left(\Delta^d \bar{\mathbf{f}}^{(n)} \right), \quad (18)$$

As was shown in Ref.⁴³, this choice is consistent with assumption on the joint probability density for the noise in the data, for which a maximum likelihood solution is equivalent to the one minimizing the norm in Equation (16).

To allow for correction of off-resonance blurring common for spiral trajectories, we incorporated the pre-measured B_0 field map into the data consistency term in Equation (9), and used time-segmented approximation with min-max interpolation for its efficient computation.²⁷ The iterations continued until the residual error relative to the data fell below a preset tolerance.

3.2 | Implementation details

Image reconstruction was implemented in MATLAB 2018 (The MathWorks, Inc.) and run on a 32-core PC with

256 Mb of RAM. The ℓ_2 problems in Equation (14) were solved using conjugate gradient descent with tolerance set to 10^{-8} using gridding approximation of the matrix-vector multiplication.²⁸ The time-segmented approximation for B_0 correction was implemented using Matlab Parallel Computing toolbox to run the computations in parallel. The reweighting updates stopped when the relative change in the Frobenius norm of W (Equation 15) between successive reweighting iterations dropped below 10^{-3} . The regularization parameters were optimized in simulations based on the minimization of the root-mean-squared error with respect to ground truth, and then guided the reconstruction of the in vivo data. The perfusion processing was performed in JIM software package (Xinapse Systems Ltd) to determine AIF and hemodynamic perfusion parameters. JIM software was also used for image processing tasks including volume co-registration and brain extraction.

3.3 | Data acquisition design

Figure 1 illustrates the proposed acquisition and reconstruction design. The pulse sequence consists of fat suppression, slice excitation, and spiral-out readout blocks (Figure 1A). Instead of using one long, single-shot readout, we opt for a trajectory that covers k-space with N shorter, N -fold undersampled spiral interleaves. For each slice, the interleaves are acquired in the bit-reversed order⁴⁵ generated by an algorithm that inverts a binary representation of each number from 0 to $N-1$ to generate a pseudo-random distribution in both temporal and TE dimensions (Figure 1B) and provides a high degree of sampling incoherency to ensure efficiency of the temporal regularization, as codified in the CS theory.⁴⁶ Thanks to the shorter readout per echo, several echoes can be acquired during the same acquisition window, with the last echo selected to match the target TE .⁴⁷ It should be noted that readout shortening also decreases TR per slice (TR_S) correspondingly, thereby allowing acquisition of a larger number of slices in each TR to cover the targeted volume and/or achieving higher temporal resolution. The volume is acquired multiple times including several dummy repetitions to reach the steady state, pre-contrast data collection for baseline image reconstruction, and time frames to track the CA passage after its injection. The pre-contrast stage is chosen to be sufficiently long for acquisition of the fully sampled, high-SNR baseline image (Figure 1C). After acquisition, the fully sampled, high-SNR baseline images are reconstructed using iterative conjugate gradients. In addition to their intended use in the calculations of perfusion maps, we use the baseline images to estimate the required calibrations. Namely, we use the highest

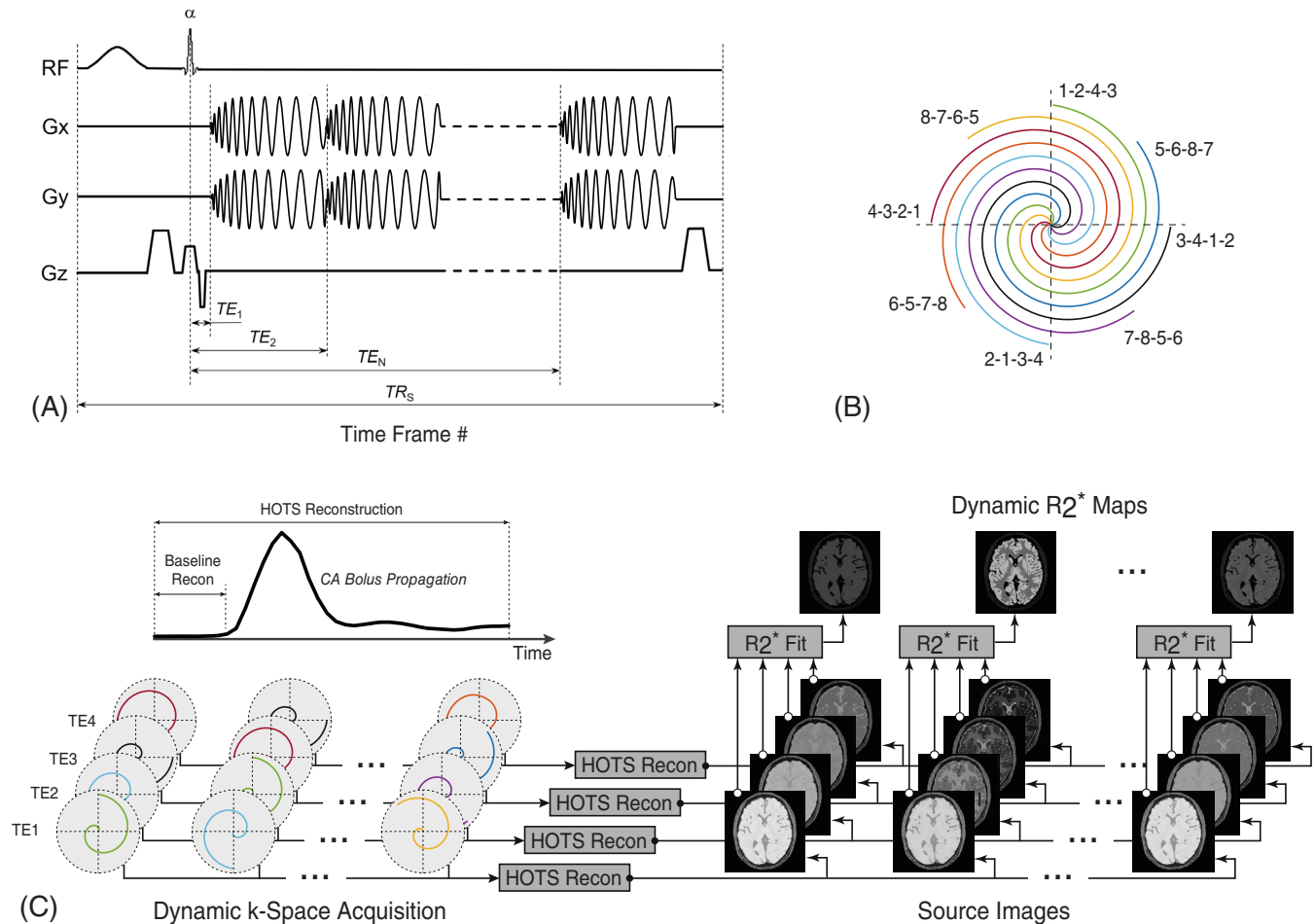


FIGURE 1 Acquisition and reconstruction design of the proposed method. (A) Pulse sequence diagram. After chemical fat saturation, the slice is selectively excited, and the free induction decay is sampled by the spiral-out interleaves at several TEs. The pulse sequence is repeated for each slice, after which it returns to the first slice and proceeds to acquire the next time frame, now with a new set of interleaves. (B) Periodic ordering of k-space coverage by spirals on the example of eight-interleaf acquisition. Sequence n1-n2-n3-n4 corresponds to the time frame numbers, in which a given spiral interleaf is acquired for echoes 1 through 4, respectively. (C) Diagram of the acquisition timing, HOTS reconstruction, and R_2^* mapping for subsequent perfusion processing. HOTS, higher order temporal smoothness.

SNR (first echo) baseline images to calculate the coil sensitivities as described in Ref.¹⁹ Further, the evolution of the image phase sampled at different TEs can be used for the B_0 mapping.⁴⁸ In our particular implementation, we estimate the B_0 map using the graph-cut technique,⁴⁹ thereby taking advantage of all TEs and regularized phase unwrapping to increase robustness of the mapping. The coil sensitivities and B_0 map are supplied to reconstruct dynamic series solving Equation (9) with a given temporal penalty on a per-echo basis (Figure 1C). Finally, all multi-echo images are fit by the exponential model yielding baseline and dynamic R_2^* maps, which in turn can be used for the perfusion processing described in the next section.

3.4 | Perfusion Processing

The R_2^* changes with respect to the baseline value,

$$\Delta R_2^* = R_2^* - R_{2,0}^*, \quad (19)$$

were converted into CA concentration $C_i(t)$ using the proportionality relationship between them.³⁶ When evaluating methods in a single-echo regime (i.e., without R_2^* mapping), a ΔR_2^* surrogate was estimated from the apparent signal changes with respect to the baseline for a given TE:

$$\Delta R_2^* = -\ln \left(\frac{S(t)}{S(0)} \right) / TE. \quad (20)$$

After the conversion, cerebral blood volume measures were obtained as an area under the $C_t(t)$ curve normalized either by the area under the AIF curve (CBV, quantitative processing) or by the averaged signal in white matter region of interest (ROI; rCBV, semi-quantitative processing to bypass AIF estimation). Additionally, in quantitative experiments, mean transit time (MTT) was determined from the tissue residue function obtained by deconvolving AIF from $C_t(t)$ (Equation 13) as previously described.³⁶ Finally, the cerebral blood flow was determined using the central volume principle³⁶:

$$\text{CBF} = \frac{\text{CBV}}{\text{MTT}} \quad (21)$$

3.5 | Simulation studies

We first evaluated the acquisition and reconstruction methods in digital phantom experiments (Figure 2). The data acquisition was simulated for a realistic digital brain model⁵⁰ (Figure 2A) with tissue parameters at 3 T⁵¹ and coil sensitivities obtained in a separate scan of a phantom object. The temporal changes (Figure 2B) were simulated using Equations (11) and (13) with AIF obtained from an in vivo exam and tissue-specific residue function for white matter (WM), gray matter (GM), and vessels, respectively.⁵² All trajectories were designed for a system with slew rate of 20 000 G/cm/s, maximum gradient of 5 G/cm, sampling rate 4 us/sample, and field-of-view 22 cm as described in⁵³ (<http://mrsrl.stanford.edu/~brian/vdspiral/>). The k-space data were computed using direct signal calculations with Equation (1). In simulations, we first compared the resolution loss due to intra-readout T_2^* decay for our four-echo and previously described two-echo spirals¹⁷ by simulating the fully sampled k-space coverage. To ensure equivalent comparisons, we assumed a realistic 2× parallel MRI acceleration in the two-echo trajectory

design to attain spirals with the last TE approaching that of the in vivo four-echo acquisition protocol and with the same nominal resolution. We simulated both standard and proposed MRI acquisitions, exactly matching most parameters of in vivo acquisition except for TE s, whose selection was guided by the minimal possible second TE of the standard protocol ($TE = 3, 42$ ms for a standard two-echo protocol and additional $TE = 16, 29$ ms for our protocol). To evaluate performance of the acquisition schemes for dynamic R_2^* values, we performed WM/GM-specific Monte Carlo (MC) simulations. Multiple instances ($n = 1000$) of signals generated from ground truth R_2^* values (Figure 2B) were corrupted with i.i.d. Gaussian noise and fit to obtain multiple R_2^* estimates. Means and SDs were evaluated across the MC R_2^* estimates.

We also carried out a series of MC experiments to separately characterize the estimation bias (accuracy) and noise (precision) in the images and R_2^* maps for different reconstruction schemes. The preliminary results of the MC experiments also guided the selection of a manageable undersampling level ($R = 8$) (and, hence, the number of interleaves), for a given coil array. Each individual reconstruction scheme was defined by the order of smoothness model ($d = 1, 2, 3$) and the type of the regularization norm ($p = 1, 2$). One-hundred realizations of complex-valued i.i.d. Gaussian noise were added to the simulated k-space data to yield the MC samples. The dynamic image series from reconstruction of each such dataset was processed to yield the maps of interest. For either a single image in the series or a quantitative map, we assessed the reconstruction bias by taking a pixelwise mean across all the reconstructed MC samples Y_k ,

$$\langle Y \rangle = \frac{1}{K} \sum_{k=1}^K Y_k,$$

and subtracting it from the ground truth reconstructed from the noiseless, fully sampled data. To yield the relative bias measures, the difference was normalized per

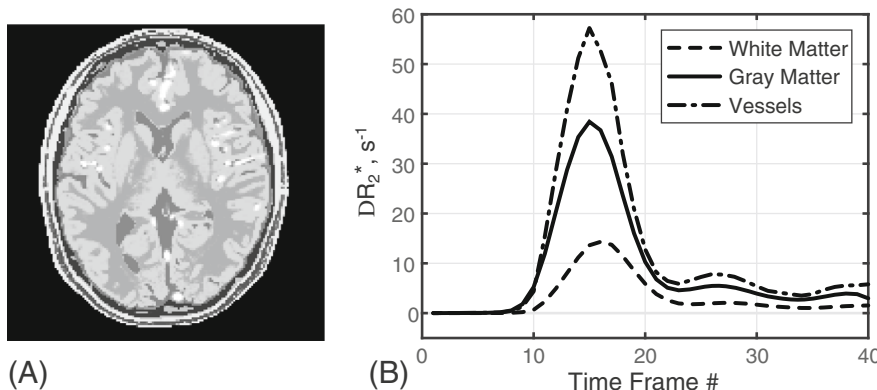


FIGURE 2 Data used in the simulation studies. (A) Digital brain model. (B) Temporal waveforms modeling the CA passage through vessels and brain tissues. The simulations assumed the proportionality of the tissue CA concentration and ΔR_2^* (R_2^* change with respect to its baseline value prior to CA injection). CA, contrast agent.

TE by the mean value of the corresponding ground truth across all time frames. We also evaluated noise propagation by calculating maps of noise SD across MC samples as follows:

$$\sigma = \sqrt{\frac{1}{K-1} \sum_{k=1}^K (\langle Y \rangle - Y_k)^2}.$$

In the absence of ground truth, the similarity of two signals x and y was assessed using root-mean-squared distance normalized by the averaged signal norms:

$$\text{nRMSD} = \frac{\|x - y\|_2}{0.5(\|x\|_2 + \|y\|_2)} \quad (22)$$

3.6 | In vivo studies

Following informed consent according to the Institutional Review Board policy at our institution, five human subjects (four females, one male, age range 24–47 y) were scanned on a 3.0T scanner (Discovery TM MR750, GE Healthcare, Waukesha, WI) with an eight-channel head coil. Structural $T1$ -weighted IR-FLASH images were collected first at 1 mm isotropic resolution. The segmented eight-interleaf, four-echo spiral sequence ($TR = 1.35$ s, $TE = 3, 15, 27, 39$ ms) was acquired for 20 consecutive 5 mm slices with matrix size 160×160 (in-plane resolution 1.375×1.375 mm²) and flip angle 60° . The timing of the trajectories followed the design in Figure 1. A bolus injection (0.2 mmol/kg of gadodiamide, Omniscan, GE Healthcare) was performed 30 s into the scan at a rate of 4 mL/s. An additional PWI dataset was acquired in one of the subjects during a separate visit using standard vendor EPI with $2 \times$ parallel MRI acceleration. EPI sequence constraints allowed scanning with the TE close to the third TE of the proposed pulse sequence ($TE = 29$ ms) and fewer slices (18 vs 20), while matching the remaining parameters of the two pulse sequences (including nominal spatial resolution, matrix size, flip angle, and TR) and locations of the overlapping slices. The single-echo processing (Equation 20) was applied to EPI data and HOTS reconstruction of the third echo to compare both methods under identical conditions. The fidelity of source images obtained with the proposed method and EPI was assessed by measuring mutual information (MI) between the source images and the corresponding structural images after co-registration.⁵⁴ The reconstruction time for the regularized approach was 76 min with B_0 correction and 13 min without B_0 correction (per slice per echo, all time frames reconstructed simultaneously).

4 | RESULTS

4.1 | Simulation-based evaluations

Figure 3 illustrates the effects of readout shortening and simultaneous increase of the number of echoes in the proposed scheme, as compared to the previously published two-echo acquisition.¹⁷ The shorter readout diminishes the $T2^*$ filtering effect, significantly improving the image resolution (Figure 3A, B). Increasing the number of echoes improves noise properties of the dynamic $R2^*$ mapping (Figure 3C). Indeed, as $R2^*$ mapping with two echoes has near-optimal sensitivity to noise errors only for a very narrow $R2^*$ range centered around one “optimal” $R2^*$ value,⁵⁵ the noise level varies significantly as $R2^*$ changes with the CA passage (Figure 3D). Using the larger number of TEs leads to a more optimal acquisition over a wider range of $R2^*$ values positively affecting noise performance of the dynamic imaging.

Figure 4 demonstrates results of MC-based evaluations of the regularization approaches for reconstruction of the multi-echo DSC-PWI images on the example of the last echo. Several trends relating the regularization design to image errors can be identified. Independently of the norm, increasing the model order reduces the bias and simultaneously increases the noise level. For a given model order, the quadratic norm ($p = 2$) yields a lower noise level than the sparsity-promoting CS norm ($p = 1$) but at the same time provides a less accurate reconstruction. The observed trends (higher accuracy and lower precision with increasing model order and going from $p = 2$ to $p = 1$) are most conspicuous for the later echoes (Supporting Information Figure S1, which is available online), i.e., for the image series with more varying temporal dynamics.

Similar trends are observed for errors of $R2^*$ estimation from the multi-echo images (Figure 5). The maps of bias and noise errors for the peak contrast frame are shown in Figure 5A. The spatial distribution of noise errors is non-uniform across WM and GM and reflects the fact that efficiency mapping depends on the $R2^*$ value in each tissue (Figure 3C). The observed trends are supported by quantitative error estimates averaged across all frames (Figure 5B). The higher-order models ($d = 2, 3$) significantly improve $R2^*$ mapping accuracy (compared to the standard first difference), with $d = 3$ providing the least bias, but at the expense of precision, and $d = 1$ providing the lowest noise. (The trends continued to the fourth order difference; results are not shown for brevity.) The omnidirectional dependence of the noise and bias errors on the model order and the norm necessitates a balanced selection of the regularization design for DSC-PWI. The simulation results suggest that the combination of the second difference ($d = 2$) with CS norm ($p = 1$) is a viable

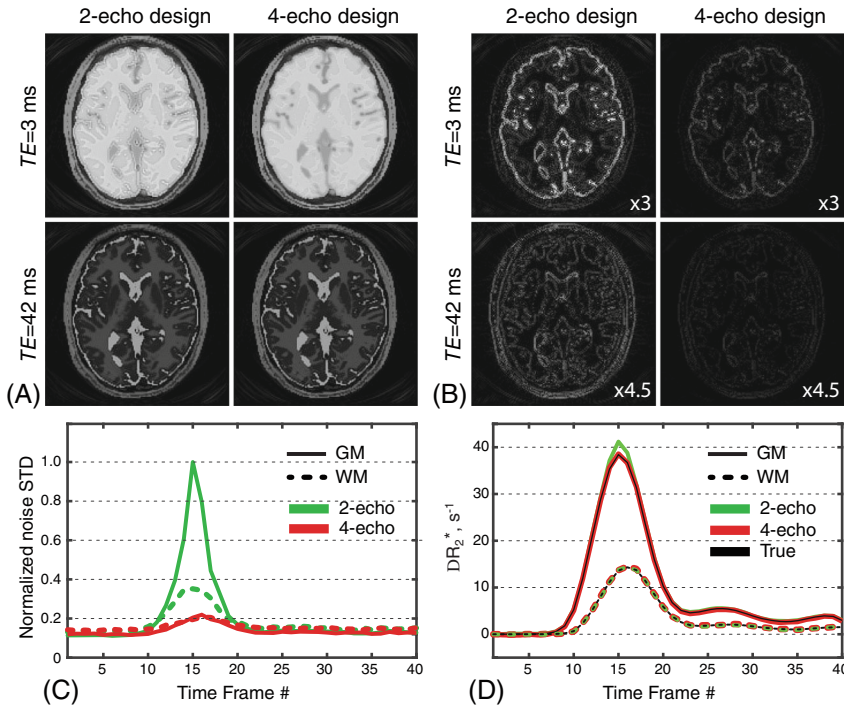


FIGURE 3 Illustration of advantages of increasing the number of echoes with simultaneous decrease of the readout duration. (A) The images corresponding to the time frame #15 (peak contrast) from the two-echo design and a subset of images at the corresponding TEs from the four-echo design. Note improved resolution of the new design due to the diminished R_2^* decay. (B) The absolute errors of images in (A) with respect to the ground truth. (C) Normalized noise SD vs. time (single-point MC simulations, normalized to peak value in GM). (D) Dynamic ΔR_2^* values from the MC simulations. Note improved noise performance of R_2^* estimation in (C) with increased number of echoes during the passage of the CA bolus (D) when the tissue R_2^* varies significantly over time. CA, contrast agent; GM, gray matter; MC, Monte Carlo.

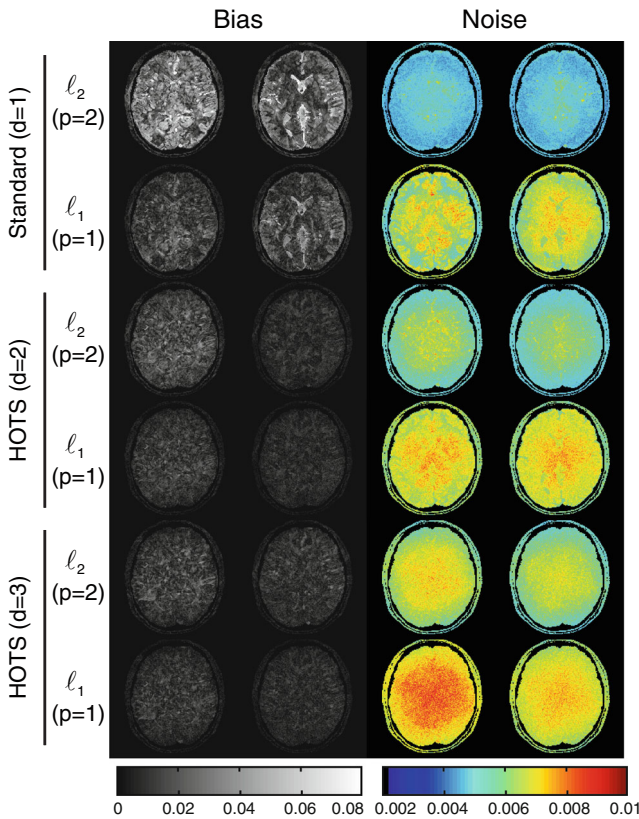


FIGURE 4 MC-based comparison of standard ($d = 1, p = 1, 2$) and HOTS ($d > 1, p = 1, 2$) penalties on the relative bias and noise SD of pre-contrast (#8, left) and peak contrast (#15, right) images for the last TE. HOTS, higher order temporal smoothness; MC, Monte Carlo.

higher-order regularization for DSC-PWI, which provides the relative bias error close to that of $d = 3$ (3.2% difference) and the noise error approaching that of $d = 1$ (2.3% difference).

4.2 | In Vivo Evaluation

Figure 6 compares effects of several reconstruction designs on the ΔR_2^* time course (Equation 19) from in vivo studies. While the first order difference ($d = 1$) regularizations recover the expected main and recirculation peaks of the CA bolus propagation, these features are notably broadened and reduced in maximum values, indicating over-smoothing by this temporal model. Increasing the model order and going from quadratic ($p = 2$) to sparsity-promoting ($p = 1$) norm alleviates the effects. Normalized distance measures (Equation 22) between the ΔR_2^* time courses reconstructed with different combinations of d and p values (Table 1) show that, as in the simulations, the effect from the sparsity-promoting norm is least pronounced for the highest ($d = 3$) model order, which suggests that using CS norms becomes less important for models capable of a more complete representation of the dynamics in the temporal series. Again, ($d = 2, p = 1$) regularization provides restoration of temporal dynamics closest to the regularization that showed the highest accuracy in simulations ($d = 3, p = 1$).

Figure 7 shows images reconstructed with and without HOTS regularization ($d = 2, p = 1$). Reconstruction

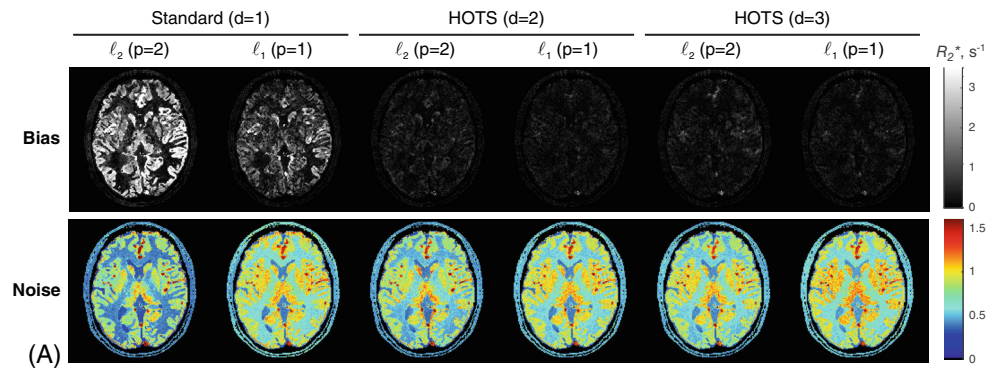


FIGURE 5 MC-based comparison of standard and HOTS penalties with respect to the accuracy and noise of the dynamic R_2^* mapping. (A) Representative bias and noise SD maps (peak contrast frame #15). (B) Bias and noise errors estimated across all time frames separately in WM and GM. GM, gray matter; HOTS, higher order temporal smoothness; MC, Monte Carlo; WM, white matter.

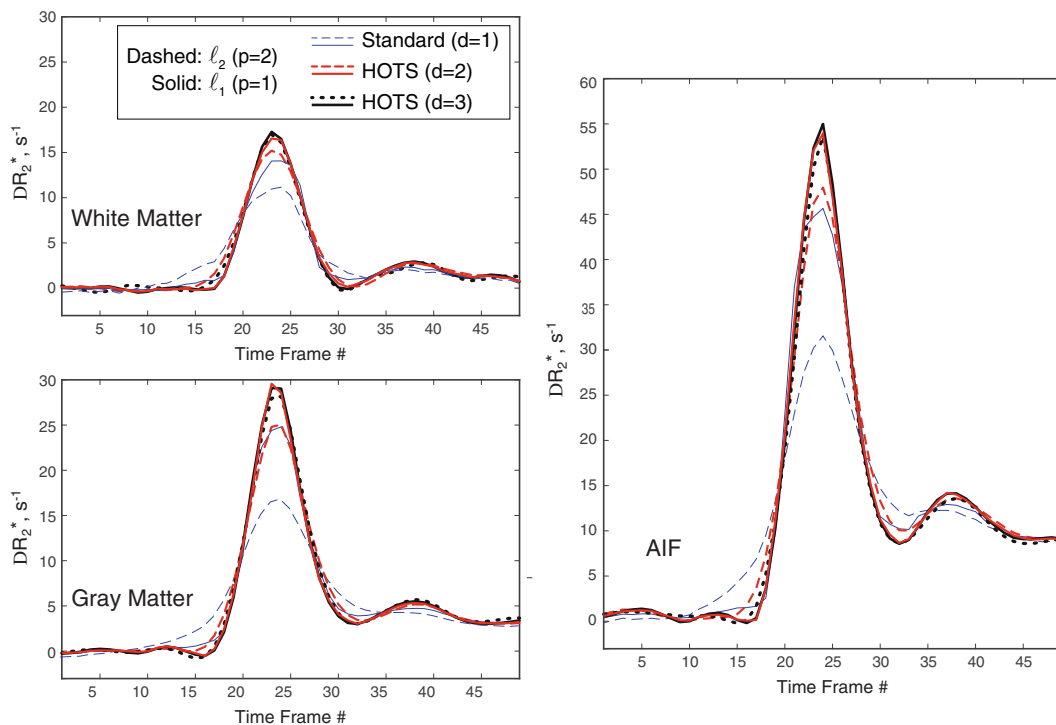
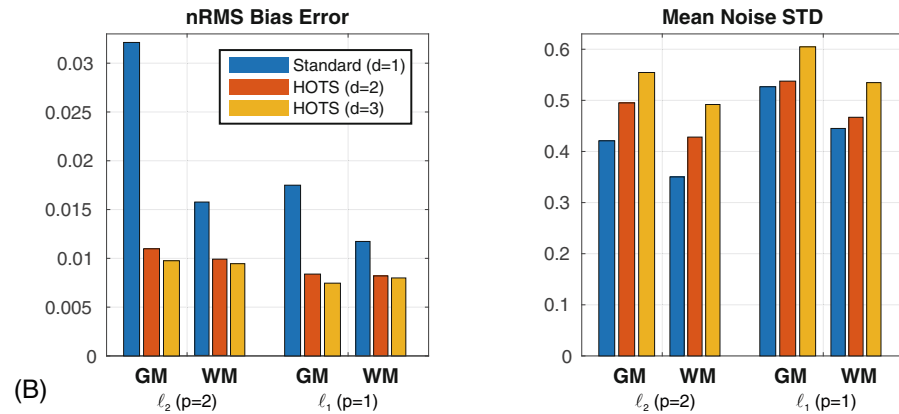


FIGURE 6 Time dependency of ΔR_2^* in white matter and gray matter and AIF from in vivo images reconstructed with different temporal smoothness regularizations. Note significant widening/decreased peak value for the standard first order regularizations ($d = 1$). Using standard TV (i.e., $d = 1, p = 1$) somewhat alleviates these effects compared to quadratic norm, but still underperforms substantially compared to HOTS regularizations with either norm. AIF, arterial input function; HOTS, higher order temporal smoothness.

TABLE 1 Pairwise similarity between temporal waveforms in GM/WM/AIF of in-vivo data reconstructed using reconstructions with different regularization approaches (A vs. B) as assessed by normalized root-mean-squared distance (Equation 22).

Recon A	Recon B				
	$d = 1, p = 2$	$d = 2, p = 1$	$d = 2, p = 2$	$d = 3, p = 1$	$d = 3, p = 2$
$d = 1, p = 1$	0.33/0.29/0.35	0.12/0.15/0.11	0.07/0.15/0.10	0.13/0.17/0.13	0.11/0.17/0.13
$d = 1, p = 2$		0.43/0.38/0.41	0.32/0.30/0.32	0.49/0.40/0.42	0.42/0.37/0.39
$d = 2, p = 1$			0.13/0.12/0.11	0.03/0.04/0.03	0.05/0.08/0.06
$d = 2, p = 2$				0.14/0.14/0.12	0.10/0.12/0.09
$d = 3, p = 1$					0.05/0.08/0.05

Abbreviations: AIF, arterial input function; GM, gray matter; WM, white matter.

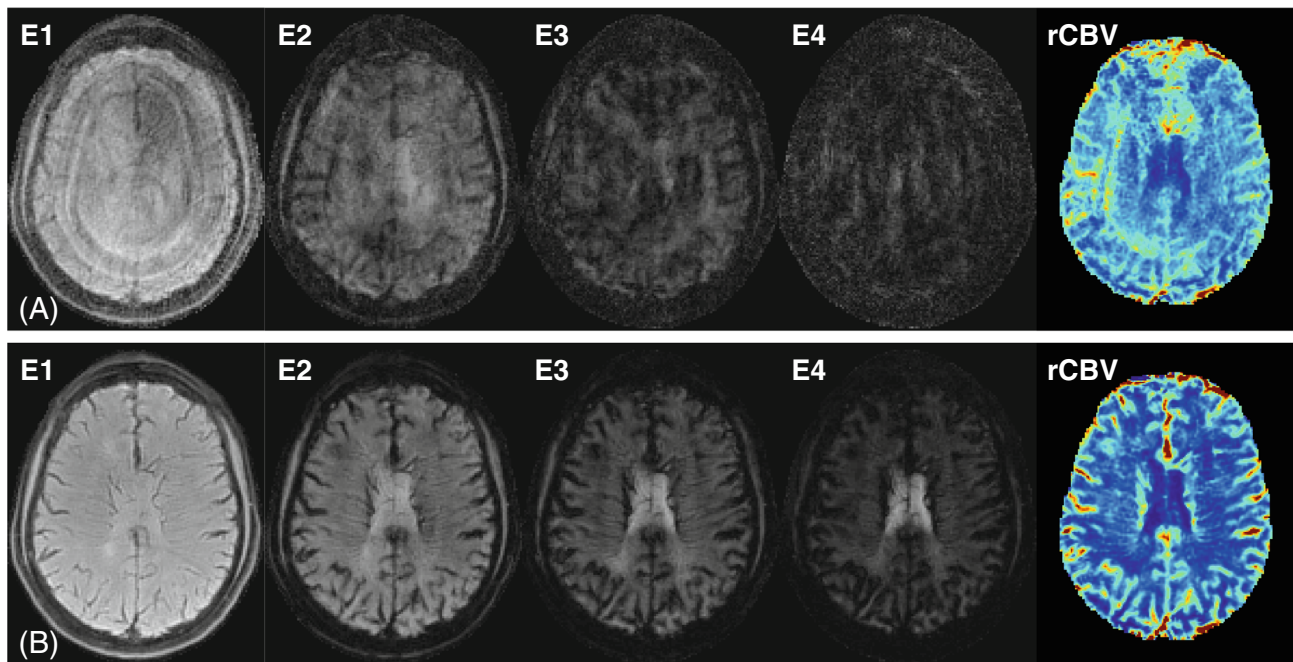


FIGURE 7 A,B, Comparison of the multi-echo spiral images for the peak contrast frame and rCBV maps obtained without (A) and with (B) HOTS regularization ($d = 2, p = 1$). Note unresolved spiral aliasing in (A) due to inability of parallel MRI alone to deal with the targeted undersampling factors ($R = 8$) for all four echoes. Note much improved image quality for the regularized reconstruction (B). HOTS, higher order temporal smoothness; rCBV, relative cerebral blood volume.

without regularization (i.e., with parallel MRI alone) is not able to support the level of undersampling arising in the proposed high-resolution, multi-echo DSC PWI (Figure 7A). Enhancing reconstruction with the proposed regularization permits higher acceleration, successfully resolving the aliasing for all TE s and resulting rCBV maps (Figure 7B). Finally, Figure 8 shows representative results from full quantitative processing of the DSC-PWI series estimated by the proposed method. The maps show excellent depiction of GM structures and medullary veins.

Figure 9 compares the quality of source images and perfusion maps obtained with standard (EPI-based) method and HOTS-regularized reconstruction of the

matching TE of the spiral data. The source images obtained with the proposed method exhibit significantly improved fidelity compared to EPI, which is reflected in 21.7% increase in MI between the source images for the proposed method and structural IR FLASH images compared to MI between the EPI source images and their corresponding IR FLASH images. The improvements pertain to image quality deficiencies commonly observed in EPI imaging, and include a remarkable reduction in image distortions, diminished signal pileups and signal dropouts, all improving the fidelity of the rCBV maps. Of special note, despite identical nominal resolution prescribed for comparison purposes, the rCBV map from the proposed

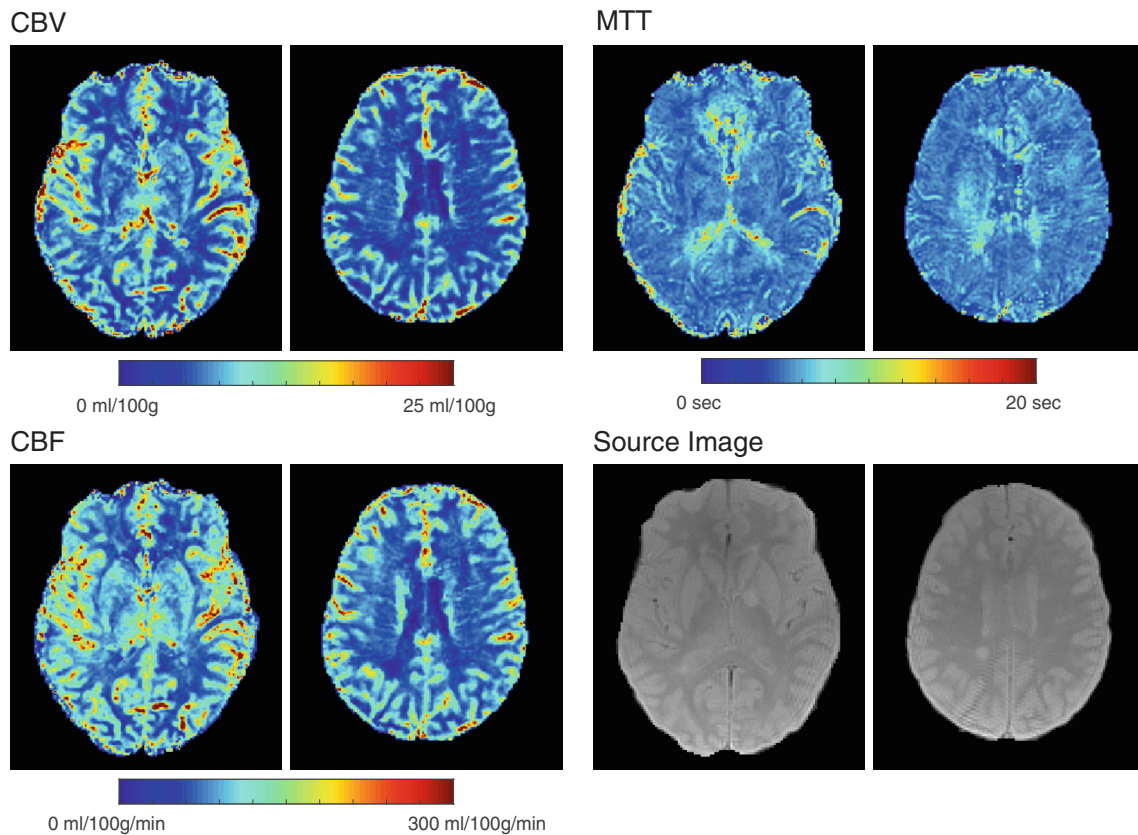
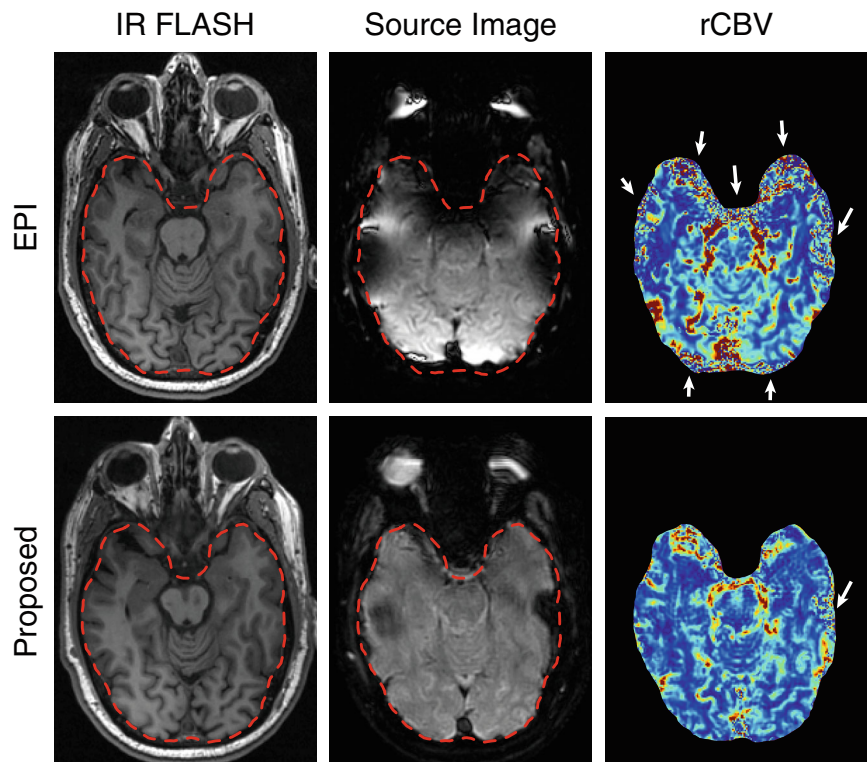


FIGURE 8 Quantitative perfusion analysis maps and anatomical reference (source) images obtained with the proposed method in two representative slice locations.

FIGURE 9 Comparison of DSC-PWI with standard (EPI) and HOTS-regularized reconstruction of the matching TE of the spiral data (the same volunteer with matching injection protocol, acquisition parameters and slice locations). Brain contours generated from the brain extraction processing of structural IR FLASH images were overlaid onto source images to assist in the evaluations. Note dramatic image quality improvement with the proposed method including diminished distortions, signal pileups and dropouts, which propagate into rCBV maps. Note an increase of apparent image resolution and decrease of vessel blooming with the proposed method. DSC-PWI, dynamic susceptibility contrast perfusion weighted imaging; EPI, echo planar imaging; rCBV, relative cerebral blood volume.



method has much higher apparent resolution, thanks to reduction of $T2^*$ filtering effects in its shorter readout. One impressive effect from the improved PSF can be observed in a dramatic reduction of vessel blooming in the new perfusion map.

5 | DISCUSSION

We have proposed herein a method that alleviates the challenges of DSC-PWI by engaging higher order temporal smoothness property of DSC-PWI signal to enable efficient multi-shot interleaved spiral acquisition over multiple TEs. The ability of the method to restore highly under-sampled data translates into remarkable improvements in image quality and resolution as compared to the standard single-echo, single-shot EPI-based DSC-PWI. While some observed EPI artifacts can be alleviated by post-processing (e.g., distortion correction using pre-acquired B_0 maps), the loss of image resolution and signal dropouts can be only alleviated by engaging shorter readouts, which is studied in this paper. The attained improvements are especially important for multi-echo implementation of DSC-PWI that may overcome many challenges associated with single-echo methods,^{14,56} but typically at the expense of image quality and resolution. For example, compared to previously described spiral multi-echo DSC-PWI design,¹⁷ our method allows a significant resolution increase (from 96×96 to 160×160) while doubling the number of echoes (from 2 to 4), enjoying a shorter readout, and allowing a near 50% increase in the number of slices (from 13 to 20), all leading to a multifold ($\sim 4.3\times$) reduction of the voxel size. The resolution gains may be particularly advantageous for existing perfusion approaches that infer contrast concentration from the image phase (Supporting Information Figure S2) using dynamic quantitative susceptibility mapping,⁵⁷ which benefits significantly from higher resolution imaging.

Our strategy of multi-shot acquisition, in which the desired readout shortening simultaneously leads to sampling a larger number of TEs, is tightly coupled with the ability of the reconstruction to support the increased undersampling factors of such datasets. To our knowledge, this paper is the first to report the utility of temporally regularized reconstruction to support the high undersampling in DSC-PWI. Temporal TV regularization ($d = 1, p = 1$) is a popular approach to accelerate many non-Cartesian dynamic imaging applications, in which no more specific prior information about signal other than its temporal regularity is available. Our results demonstrate that engaging higher order temporal smoothness may be more beneficial to support higher undersampling in applications with rapid dynamic changes such as DSC-PWI. Higher order

differences studied in the paper ($d = 2,3$) provide increasingly more accurate models for DSC-PWI, with further accuracy gains afforded by CS (ℓ_1) rather than quadratic (ℓ_2) norm. The observed trends in performance improvement, along with previously published evidence on utility of the total generalized variation in cardiac imaging,²⁵ support that higher order differences may be beneficial not only for previously described spatial^{58–60} but also for temporal regularizations, thereby potentially benefiting a wider range of dynamic applications. However, our results on the regularization-dependent noise amplification suggest that optimization of the reconstruction scheme for a given application should consider desired spatial and temporal resolutions (and associated undersampling factors), trajectory properties, available SNR, and finally, desired tradeoffs between accuracy and precision. Specifically, in the context of DSC-PWI, using ($d = 2, p = 1$) appears to be beneficial both from accuracy and noise points of view, though using higher ($d = 3$) difference may also perform adequately even without engagement of CS norm.

The applicability of other modern reconstruction approaches to DSC-PWI may face a separate set of challenges and requires additional investigation. The multi-echo acquisition may allow estimation of dynamic $R2^*$ maps from the undersampled data directly (i.e., without reconstruction of source images).⁶¹ This may eliminate the residual $R2^*$ blurring (Figure 3A, B) and allow tackling higher undersampling factors. However, combining the direct parameter mapping with temporal constraints may lead to a very large non-linear joint optimization problem, which may be challenging to solve both algorithmically and computationally. Next, the temporal dimension can also be parametrized using the prior knowledge that contrast propagation dynamics can be modeled as a linear combination of gamma-variate functions.⁶² In addition to the general feasibility concerns of the nonlinear model-based approaches to DSC-PWI described above, such model-based extension may face additional estimation and convergence problems due to the large number of parameters (eight for modeling main CA bolus propagation and first recirculation). Next, methods based on the partial separability^{33,34} rely on full sampling of k-space center in each temporal frame, which may require the use of less efficient variable-density spiral trajectories. Finally, the use of other related methods based on low-rank matrix completion⁶³ faces the problem of existence of matrix completion algorithms for non-Cartesian acquisitions.

One limitation of the reconstruction approach is its potential sensitivity to motion, which may disrupt the temporal continuity of the signal and invalidate the smoothness assumption in restless subjects. Incorporating motion correction into the reconstruction is a standard approach

to alleviate such limitations, but may require modifications of reconstruction and/or acquisition for simultaneous^{64,65} or navigator-based^{66,67} estimation of motion parameters. Deviation of the actual spiral k-space trajectory from a nominal one due to system imperfections may cause data inconsistencies between different spiral interleaves, potentially affecting the smoothness model and hence reconstruction performance, especially for later echoes. This may be overcome by pre-calibrating the trajectories and using the measured trajectories instead of nominal ones.^{68–71} The current implementation does not account for intrinsic blurring of spiral multi-echo images, which are used to estimate the B_0 map. Using joint estimation may alleviate the problem, potentially leading to more accurate self-calibrated B_0 estimates.⁷² One interesting extension may be the use of spiral-in trajectories to further reduce the acquisition time per slice,⁷³ attaining the targeted time for the last echo, at the expense of one echo in the echo train. Increasing the number of coil elements may promote even higher accelerations.⁷⁴ Combination of the method with simultaneous-multi-slice imaging may further improve slice resolution and coverage.⁷⁵ This remains a subject of future work.

ACKNOWLEDGMENTS

This work was supported by NIH (R21EB018483, R01EB027087, P30CA014520) and GE Healthcare.

DATA AVAILABILITY STATEMENT

The MATLAB code and a sample dataset are available online (<https://github.com/velikina/DSC-PWI>).

ORCID

Julia V. Velikina  <https://orcid.org/0000-0002-2058-8601>
Alexey A. Samsonov  <https://orcid.org/0000-0003-1966-3034>

REFERENCES

- Rosen BR, Belliveau JW, Vevea JM, Brady TJ. Perfusion imaging with NMR contrast agents. *Magn Reson Med*. 1990;14:249-265.
- Mlynash M, Olivot JM, Tong DC, et al. Yield of combined perfusion and diffusion MR imaging in hemispheric TIA. *Neurology*. 2009;72:1127-1133.
- Sorensen AG, Buonanno FS, Gonzalez RG, et al. Hyperacute stroke: evaluation with combined multisection diffusion-weighted and hemodynamically weighted echo-planar MR imaging. *Radiology*. 1996;199:391-401.
- Hakymez B, Erdogan C, Ercan I, Ergin N, Uysal S, Atahan S. High-grade and low-grade gliomas: differentiation by using perfusion MR imaging. *Clin Radiol*. 2005;60:493-502.
- Kruser TJ, Mehta MP, Robins HI. Pseudoprogression after glioma therapy: a comprehensive review. *Expert Rev Neurother*. 2013;13:389-403.
- Quarles CC, Schmainda KM. Assessment of the morphological and functional effects of the anti-angiogenic agent SU11657 on 9L gliosarcoma vasculature using dynamic susceptibility contrast MRI. *Magn Reson Med*. 2007;57:680-687.
- Sawhani RN, Raizer J, Horowitz SW, et al. Glioblastoma: a method for predicting response to antiangiogenic chemotherapy by using MR perfusion imaging--pilot study. *Radiology*. 2010;255:622.
- Law9 M, Young RJ, Babb JS, et al. Gliomas: predicting time to progression or survival with cerebral blood volume measurements at dynamic susceptibility-weighted contrast-enhanced perfusion MR imaging. *Radiology*. 2008;247:490-498.
- Ellinger R, Kremser C, Schocke MF, et al. The impact of peak saturation of the arterial input function on quantitative evaluation of dynamic susceptibility contrast-enhanced MR studies. *J Comput Assist Tomogr*. 2000;24:942-948.
- Bjornerud A, Sorensen AG, Mouridsen K, Emblem KE. T1- and T2*-dominant extravasation correction in DSC-MRI: part I-theoretical considerations and implications for assessment of tumor hemodynamic properties. *J Cereb Blood Flow Metab*. 2011;31:2041-2053.
- Quarles CC, Ward BD, Schmainda KM. Improving the reliability of obtaining tumor hemodynamic parameters in the presence of contrast agent extravasation. *Magn Reson Med*. 2005;53:1307-1316.
- Newbould RD, Skare ST, Jochimsen TH, et al. Perfusion mapping with multiecho multishot parallel imaging EPI. *Magn Reson Med*. 2007;58:70-81.
- Vonken EJ, van Osch MJ, Bakker CJ, Viergever MA. Measurement of cerebral perfusion with dual-echo multi-slice quantitative dynamic susceptibility contrast MRI. *J Magn Reson Imaging*. 1999;10:109-117.
- Stokes AM, Semmineh NB, Nespodzany A, Bell LC, Quarles CC. Systematic assessment of multi-echo dynamic susceptibility contrast MRI using a digital reference object. *Magn Reson Med*. 2020;83:109-123.
- Schmiedeskamp H, Andre JB, Straka M, et al. Simultaneous perfusion and permeability measurements using combined spin- and gradient-echo MRI. *J Cereb Blood Flow Metab*. 2013;33:732-743.
- Paulson ES, Schmainda KM. Comparison of dynamic susceptibility-weighted contrast-enhanced MR methods: recommendations for measuring relative cerebral blood volume in brain tumors. *Radiology*. 2008;249:601-613.
- Paulson ES, Prah DE, Schmainda KM. Spiral Perfusion Imaging with Consecutive Echoes (SPICE) for the simultaneous mapping of DSC- and DCE-MRI parameters in brain tumor patients: theory and initial feasibility. *Tomography*. 2016;2:295-307.
- Yudilevich E, Stark H. Spiral sampling in magnetic resonance imaging-the effect of inhomogeneities. *IEEE Trans Med Imaging*. 1987;6:337-345.
- Pruessmann KP, Weiger M, Scheidegger MB, Boesiger P. SENSE: sensitivity encoding for fast MRI. *Magn Reson Med*. 1999;42:952-962.
- Tsao J, Kozerke S. MRI temporal acceleration techniques. *J Magn Reson Imaging*. 2012;36:543-560.
- Christodoulou AG, Zhang H, Zhao B, Hitchens TK, Ho C, Liang ZP. High-resolution cardiovascular MRI by integrating parallel imaging with low-rank and sparse modeling. *IEEE Trans Biomed Eng*. 2013;60:3083-3092.
- Adluru G, McGann C, Speier P, Kholmovski EG, Shaaban A, Dibella EV. Acquisition and reconstruction of undersampled

- radial data for myocardial perfusion magnetic resonance imaging. *J Magn Reson Imaging*. 2009;29:466-473.
23. Feng L, Grimm R, Block KT, et al. Golden-angle radial sparse parallel MRI: combination of compressed sensing, parallel imaging, and golden-angle radial sampling for fast and flexible dynamic volumetric MRI. *Magn Reson Med*. 2014;72:707-717.
 24. Lingala SG, Jacob M. Blind compressive sensing dynamic MRI. *IEEE Trans Med Imaging*. 2013;32:1132-1145.
 25. Schloegl M, Holler M, Schwarzl A, Bredies K, Stollberger R. Infimal convolution of total generalized variation functionals for dynamic MRI. *Magn Reson Med*. 2017;78:142-155.
 26. Adluru G, Awate SP, Tasdizen T, Whitaker RT, Dibella EV. Temporally constrained reconstruction of dynamic cardiac perfusion MRI. *Magn Reson Med*. 2007;57:1027-1036.
 27. Sutton BP, Noll DC, Fessler JA. Fast, iterative image reconstruction for MRI in the presence of field inhomogeneities. *IEEE Trans Med Imaging*. 2003;22:178-188.
 28. Pruessmann KP, Weiger M, Bornert P, Boesiger P. Advances in sensitivity encoding with arbitrary k-space trajectories. *Magn Reson Med*. 2001;46:638-651.
 29. Tarantola A. *Inverse Problem Theory and Methods for Model Parameter Estimation*. Vol xii. Society for Industrial and Applied Mathematics; 2005:342.
 30. Candes EJ, Wakin MB, Boyd SP. Enhancing sparsity by reweighted L(1) minimization. *J Fourier Anal Appl* 2008;14(5-6):877-905.
 31. Lustig M, Donoho D, Pauly JM. Sparse MRI: the application of compressed sensing for rapid MR imaging. *Magn Reson Med*. 2007;58:1182-1195.
 32. Kijowski R, Rosas H, Samsonov A, King K, Peters R, Liu F. Knee imaging: rapid three-dimensional fast spin-echo using compressed sensing. *J Magn Reson Imaging*. 2017;45:1712-1722.
 33. Liang ZP. Spatiotemporal imaging with partially separable functions. Paper presented at: Proceedings of IEEE International Symposium on Biomedical Imaging: From Nano to Macro; 2007; Arlington, VA: 988-991.
 34. Velikina JV, Samsonov AA. Reconstruction of dynamic image series from undersampled MRI data using data-driven model consistency condition (MOCCO). *Magn Reson Med*. 2015;74:1279-1290.
 35. Simonsen CZ, Ostergaard L, Vestergaard-Poulsen P, Rohl L, Bjrnerud A, Gyldensted C. CBF and CBV measurements by USPIO bolus tracking: reproducibility and comparison with Gd-based values. *J Magn Reson Imaging*. 1999;9:342-347.
 36. Ostergaard L, Weisskoff RM, Chesler DA, Gyldensted C, Rosen BR. High resolution measurement of cerebral blood flow using intravascular tracer bolus passages. Part I: mathematical approach and statistical analysis. *Magn Reson Med*. 1996;36:715-725.
 37. Benner T, Heiland S, Erb G, Forsting M, Sartor K. Accuracy of gamma-variate fits to concentration-time curves from dynamic susceptibility-contrast enhanced MRI: influence of time resolution, maximal signal drop and signal-to-noise. *Magn Reson Imaging*. 1997;15:307-317.
 38. Pinkus A. N-widths of Sobolev spaces in L^p . *Constr Approx*. 1985;1:15-62.
 39. Kolmogoroff A. About the best convergences of functions of a given function class. *Ann Math*. 1936;37:107-110.
 40. Micchelli CA, Pinkus A. Some problems in approximation of functions of 2 variables and N-widths of integral-operators. *J Approx Theory*. 1978;24:51-77.
 41. Melkman AA, Micchelli CA. Spline spaces are optimal for L2 normal-width. *Illinois J Math*. 1978;22:541-564.
 42. Beaton AE, Tukey JW. Fitting of power-series, meaning polynomials, illustrated on band-spectroscopic data. *Dent Tech*. 1974;16:147-185.
 43. Bube KP, Langanz RT. Hybrid L1/L2 minimization with applications to tomography. *Geophysics*. 1997;62:1183-1195.
 44. Charbonnier P, BlancFeraud L, Aubert G, Barlaud M. Deterministic edge-preserving regularization in computed imaging. *IEEE Trans Image Process*. 1997;6:298-311.
 45. Theilmann RJ, Gmitro AF, Altbach MI, Trouard TP. View-ordering in radial fast spin-echo imaging. *Magn Reson Med*. 2004;51:768-774.
 46. Candes EJ, Tao T. Decoding by linear programming. *IEEE Trans Inform Theory*. 2005;51:4203-4215.
 47. Willats L, Calamante F. The 39 steps: evading error and deciphering the secrets for accurate dynamic susceptibility contrast MRI. *NMR Biomed*. 2012;26:913-931.
 48. Schneider E, Glover G. Rapid in vivo proton shimming. *Magn Reson Med*. 1991;18:335-347.
 49. Hernando D, Kellman P, Haldar JP, Liang ZP. Robust water/fat separation in the presence of large field inhomogeneities using a graph cut algorithm. *Magn Reson Med*. 2010;63:79-90.
 50. Collins DL, Zijdenbos AP, Kollokian V, et al. Design and construction of a realistic digital brain phantom. *IEEE Trans Med Imaging*. 1998;17:463-468.
 51. Stanisz GJ, Odobina EE, Pun J, et al. T1, T2 relaxation and magnetization transfer in tissue at 3T. *Magn Reson Med*. 2005;54:507-512.
 52. Wong KK, Tam CP, Ng M, Wong ST, Young GS. Improved residue function and reduced flow dependence in MR perfusion using least-absolute-deviation regularization. *Magn Reson Med*. 2009;61:418-428.
 53. Lee JH, Hargreaves BA, Hu BS, Nishimura DG. Fast 3D imaging using variable-density spiral trajectories with applications to limb perfusion. *Magn Reson Med*. 2003;50:1276-1285.
 54. Maes F, Collignon A, Vandermeulen D, Marchal G, Suetens P. Multimodality image registration by maximization of mutual information. *IEEE Trans Med Imaging*. 1997;16:187-198.
 55. Atkinson AC, Donev AN. *Optimum experimental designs*. Vol xv. Clarendon Press; Oxford University Press; 1992:328.
 56. Stokes AM, Rangunathan S, Robison RK, et al. Development of a spiral spin- and gradient-echo (spiral-SAGE) approach for improved multi-parametric dynamic contrast neuroimaging. *Magn Reson Med*. 2021;86:3082-3095.
 57. Xu B, Spincemaille P, Liu T, et al. Quantification of cerebral perfusion using dynamic quantitative susceptibility mapping. *Magn Reson Med*. 2015;73:1540-1548.
 58. Hu Y, Jacob M. Higher degree total variation (HDTV) regularization for image recovery. *IEEE Trans Image Process*. 2012;21:2559-2571.
 59. Hu Y, Ongie G, Ramani S, Jacob M. Generalized higher degree total variation (HDTV) regularization. *IEEE Trans Image Process*. 2014;23:2423-2435.
 60. Knoll F, Bredies K, Pock T, Stollberger R. Second order total generalized variation (TGV) for MRI. *Magn Reson Med*. 2011;65:480-491.

61. Block KT, Uecker M, Frahm J. Model-based iterative reconstruction for radial fast spin-echo MRI. *IEEE Trans Med Imaging*. 2009;28:1759-1769.
62. Velikina JV, Samsonov AA. Application-specific compressed sensing for improved spatial and temporal resolution of intracranial CE MRA. *Proc of ISMRM*. Toronto, Canada; 2015:3790.
63. Chiew M, Smith SM, Koopmans PJ, Graedel NN, Blumensath T, Miller KL. K-t FASTER: acceleration of functional MRI data acquisition using low rank constraints. *Magn Reson Med*. 2015;74:353-364.
64. Fessler JA. Optimization transfer approach to joint registration/reconstruction for motion-compensated image reconstruction. Paper presented at: Proceedings of IEEE International Symposium on Biomedical Imaging: From Nano to Macro; 2010; Rotterdam, Netherlands: 596-599.
65. Haskell MW, Cauley SF, Wald LL. Targeted motion estimation and reduction (TAMER): data consistency based motion mitigation for MRI using a reduced model joint optimization. *IEEE Trans Med Imaging*. 2018;37:1253-1265.
66. Bammer R, Aksoy M, Liu C. Augmented generalized SENSE reconstruction to correct for rigid body motion. *Magn Reson Med*. 2007;57:90-102.
67. Johnson KO, Robison RK, Pipe JG. Rigid body motion compensation for spiral projection imaging. *IEEE Trans Med Imaging*. 2011;30:655-665.
68. Duyn JH, Yang Y, Frank JA, van der Veen JW. Simple correction method for k-space trajectory deviations in MRI. *J Magn Reson*. 1998;132:150-153.
69. Robison RK, Devaraj A, Pipe JG. Fast, simple gradient delay estimation for spiral MRI. *Magn Reson Med*. 2010;63:1683-1690.
70. Vannesjo SJ, Graedel NN, Kasper L, et al. Image reconstruction using a gradient impulse response model for trajectory prediction. *Magn Reson Med*. 2016;76:45-58.
71. Robison RK, Li Z, Wang D, Ooi MB, Pipe JG. Correction of B0 eddy current effects in spiral MRI. *Magn Reson Med*. 2019;81:2501-2513.
72. Sutton BP, Noll DC, Fessler JA. Dynamic field map estimation using a spiral-in/spiral-out acquisition. *Magn Reson Med*. 2004;51:1194-1204.
73. Bornert P, Aldefeld B, Eggers H. Reversed spiral MR imaging. *Magn Reson Med*. 2000;44:479-484.
74. Ramb R, Mader I, Jung B, Hennig J, Zaitsev M. High resolution CBV assessment with PEAK-EPI: k-t-undersampling and reconstruction in echo planar imaging. *Magn Reson Med*. 2017;77:2153-2166.
75. Barth M, Breuer F, Koopmans PJ, Norris DG, Poser BA. Simultaneous multislice (SMS) imaging techniques. *Magn Reson Med*. 2016;75:63-81.

SUPPORTING INFORMATION

Additional supporting information may be found in the online version of the article at the publisher's website.

Figure S1. MC-based comparison of standard ($d = 1$, $p = 1,2$) and HOTS ($d > 1$, $p = 1,2$) penalties on the relative bias and noise standard deviation of pre-contrast (#8, left) and peak contrast (#15, right) images for all echo times.

Figure S2. Top row: representative phase images for baseline, peak contrast, and post-contrast frames of a HOTS ($d = 2$, $p = 1$) time series reconstruction of in-vivo spiral data (the third echo time). **Bottom row:** the corresponding difference with pre-contrast phase. Note that bolus propagation causes significant changes in the image phase due to modulation of the tissue magnetic susceptibility by paramagnetic contrast agent.

How to cite this article: Velikina JV, Jung Y, Field AS, Samsonov AA. High-resolution dynamic susceptibility contrast perfusion imaging using higher-order temporal smoothness regularization. *Magn Reson Med*. 2023;89:112-127. doi: 10.1002/mrm.29425